arXiv:2610.38701v1 [quant-ph] 28 Oct 2026

Sample-Based Quantum Diagonalization for Variable Molecular Geometries

Matthieu Fortin-Deschênes*[1] and Ibrahim Shehzad[2]

[1]PINQ[2], Sherbrooke, QC J1K 1B7, Canada
[2]IBM Quantum, Thomas J. Watson Research Center, Yorktown Heights, NY 10598, USA

Abstract

Quantum and hybrid quantum-classical algorithms have the potential to improve the accuracy and scale of quantum chemistry and impact a broad range of applications such as drug discovery and catalysis. In particular, subspace methods such as sample-based quantum diagonalization (SQD) can already tackle classically challenging systems. However, practical algorithms that go beyond the computation of electronic ground and excited states are still scarce. Here, we introduce the variable-geometry sample-based quantum diagonalization (VGSQD) algorithm, which extends SQD to variable molecular geometries by reusing quantum samples from a reference geometry at displaced ones, thus significantly reducing quantum computational cost. Using circuits of up to 124 qubits on `ibm-quebec`, an IBM Heron `r2` quantum processor, we determine the equilibrium geometry and energy of the weakly bound, strongly correlated beryllium dimer, as well as the water molecule. Finally, we extend VGSQD to chemical reactions and compute the minimum energy path and energy barrier of a hydrogen exchange reaction. The results are comparable with state-of-the-art classical methods such as CCSD(T) and DMRG. This work broadens the scope of quantum algorithms for chemistry, from energies to geometry optimization and reaction pathways, both essential for practical applications.

Introduction

Quantum chemistry is widely regarded as one of the most promising applications of quantum computing. Quantum algorithms such as quantum phase estimation[1,2] and hybrid algorithms such as the variational quantum eigensolver[3–5] emerged first as important building blocks for future fault-tolerant and near-term devices, respectively. While noise hinders the application of the former to problems of a meaningful size, the latter is hampered by measurement overhead and optimization difficulties. On the other hand, subspace methods recently emerged as leading candidates for near-term and early fault tolerant devices, owing to their applicability to problems requiring large number of qubits, and their potential to improve together with the quantum hardware[6,7]. By preparing and probing a quantum state with overlap with the ground state on a Quantum Processing Unit (QPU), these methods allow the construction of a subspace onto which the Hamiltonian is projected and diagonalized at a reduced classical cost. Algorithms such as sample-based quantum diagonalization (SQD)[8], which builds on quantum-selected configuration interaction[9] have been particularly successful. In fact, together with algorithms that leverage them[10–14], they already allow

*Email: matthieu.fortin-deschenes@pinq2.com

for ground and excited state calculations of classically challenging molecules and have been applied to several use cases[15–21], such as solvated molecules and larger biological molecules.

While subspace methods have demonstrated their capability for ground and excited state computations, it is critical to develop algorithms that enable their application to practical quantum chemistry workflows. For instance, Kaliakin et al. demonstrated the use of implicit solvent methods to model molecule-solvent interactions[16]. Another key component of chemistry workflows is the modeling of molecules with variable nuclear coordinates. This is necessary to carry out structural relaxation of molecules to find their equilibrium geometry, as well as to find the minimum energy path (MEP) and energy barrier of chemical reactions. In a naive SQD approach, each molecular geometry requires its own round of circuit execution and sampling, thus the QPU cost grows with the number of geometries visited and the workflow involves frequent alternation between quantum and classical resources. To reduce the number of required quantum circuit executions, we developed the variable geometry sample-based quantum diagonalization (VGSQD) algorithm. Analogous to correlated sampling in quantum Monte Carlo, which uses sampled configurations of a reference at displaced geometries[22], VGSQD reuses quantum samples for multiple molecular geometries, thus significantly reducing the number of quantum circuit executions.

First, we describe how VGSQD extends SQD by reusing bitstrings sampled on a QPU across multiple closely related molecular geometries, and we introduce two criteria to assess when such reuse is justified. We then apply VGSQD to the structural relaxation of small molecules using a quantum-centric supercomputing workflow leveraging an IBM Heron `r2` quantum processor (`ibm-quebec`) and a high-performance computing cluster (*Harfang*). The computations are done using the cc-pVDZ and cc-pVTZ basis sets, with circuits of up to 62 and 124 qubits respectively. We first consider Be_2, whose unusual bonding makes its equilibrium bond length notoriously difficult to model. Geometry optimization with VGSQD yields relaxed bond lengths that are closer to the experimental value than those obtained with CCSD(T) for both basis sets. As for the ground state energy, the value for the relaxed Be_2 molecule is lower than DMRG and CCSD(T) for cc-pVDZ and on par with CCSD for cc-pVTZ. We then consider H_2O, which has more nuclear degrees of freedom to optimize. With the larger basis set (cc-pVTZ), the bond lengths and bond angles converge within 0.002 Å and 0.5° of the experimental values. Finally, we demonstrate the application of VGSQD to the study of chemical reactions by combining it with the climbing-image nudged elastic band (CI-NEB)[23–25] method to compute the minimum energy path and energy barrier of the $H_2 + H \rightarrow H + H_2$ hydrogen exchange reaction. The obtained saddle point geometry and barrier height are within 0.2 kcal/mol and 0.001 Å of the FCI reference, thus demonstrating the potential of VGSQD to broaden the scope of quantum computing algorithms to chemical reactions on near-term quantum hardware.

Methods

We work within the Born-Oppenheimer approximation and represent the electronic Hamiltonian in second quantization in the basis of Hartree-Fock molecular orbitals (MOs) ϕ_p obtained from either restricted Hartree-Fock (RHF) for closed-shell systems (Be_2 and H_2O) or restricted open-shell Hartree-Fock (ROHF) for open-shell systems (H_2 + H), computed with PySCF[26]. The lowest n_{frozen} MOs are kept doubly occupied and frozen, and the calculation is carried out in the active space spanned by the remaining N orbitals. In chemists' notation for the two-electron integrals, $(pq|rs) \equiv \iint \phi_p^*(\mathbf{r}_1)\,\phi_q(\mathbf{r}_1)\,r_{12}^{-1}\,\phi_r^*(\mathbf{r}_2)\,\phi_s(\mathbf{r}_2)\,d\mathbf{r}_1\,d\mathbf{r}_2$, the Hamiltonian reads:

$$\hat{H} = E_{\text{core}} + \sum_{pq\in\text{active}} \sum_{\sigma} h_{pq}^{\text{eff}}\,\hat{a}_{p\sigma}^\dagger \hat{a}_{q\sigma} + \frac{1}{2} \sum_{pqrs\in\text{active}} \sum_{\sigma\tau} (pq|rs)\,\hat{a}_{p\sigma}^\dagger \hat{a}_{r\tau}^\dagger \hat{a}_{s\tau} \hat{a}_{q\sigma}, \tag{1}$$

where a_{xy} ($a^\dagger_{xy}$) represent the annihilation (creation) operators, p, q, r, s label spatial MOs, $\sigma, \tau \in \{\alpha, \beta\}$ label spin, h^{eff}_{pq} are the effective active space one-electron (kinetic plus electron-nuclear attraction) integrals[a], and E_{core} is the nuclear repulsion energy, including the frozen core energy.

We seek the ground state, $|\Psi_0\rangle$, of this Hamiltonian, as a linear combination of Slater determinants $|\Phi_I\rangle$ (with CI coefficients c_I), which form a basis for the antisymmetric N-fermion Hilbert space:

$$|\Psi_0\rangle = \sum_I c_I \, |\Phi_I\rangle \tag{2}$$

Quantum circuits and diagonalization

For ground state calculation of the reference molecule, we use the sample-based quantum diagonalization approach. We first prepare $|\Psi_{\text{QC}}\rangle$, a state whose support in the computational basis overlaps with the support of the true ground state $|\Psi_0\rangle$ of the reference molecule. We then sample from it, i.e., we draw the set $\tilde{\chi} = \{x | x \sim \tilde{P}(x)\}$, where $x \in \{0,1\}^{2N}$ are bitstrings distributed according to the noisy distribution $\tilde{P}(x)$, which approximates the ideal distribution $P(x) = |\langle x|\Psi_{\text{QC}}\rangle|^2$ in the noiseless limit. Fermionic modes are mapped to qubits with the Jordan-Wigner transformation [27], using $2N$ qubits for N active spatial orbitals. The first N qubits encode the occupations of the spin-β orbitals and the last N qubits those of the spin-α orbitals, so that each measured bitstring corresponds directly to a Slater determinant of the active space.

To prepare the sampled state, we use the truncated local unitary cluster Jastrow (LUCJ) ansatz [28–30]:

$$|\Psi_{\text{QC}}\rangle = \hat{U} \, |x_{\text{RHF}}\rangle = e^{\hat{K}_2} e^{\hat{K}_1} e^{i\hat{J}_1} e^{-\hat{K}_1} \, |x_{\text{RHF}}\rangle \tag{3}$$

where $|x_{\text{RHF}}\rangle$ is the restricted Hartree-Fock determinant (ROHF for open-shell), $\hat{K}_\mu$ are one-body operators, whose exponentials are orbital rotations and $\hat{J}_\mu$ are density-density operators, as defined by:

$$\hat{K}_\mu = \sum_{pq,\sigma} K^\mu_{pq} \, \hat{a}^\dagger_{p\sigma} \hat{a}_{q\sigma}, \qquad \hat{J}_\mu = \sum_{pq,\sigma\tau} J^\mu_{p\sigma,q\tau} \, \hat{n}_{p\sigma} \hat{n}_{q\tau} \tag{4}$$

The ansätze are prepared using the ffsim library [31] and their parameters are obtained from CCSD calculations, with no further optimization, following previous SQD studies [8,10]. For closed-shell molecules the spin-balanced form ($J_{\alpha\alpha} = J_{\beta\beta}$, $J_{\alpha\beta} = J_{\beta\alpha}$) is used; for open-shell molecules, the spin-unbalanced form with independent $J_{\alpha\alpha}$, $J_{\beta\beta}$ and $J_{\alpha\beta}$ and ROHF-based CCSD amplitudes are used. The α and β spin orbitals are each mapped to individual qubit chains, with both chains coupled together through ancilla qubits. The 156 qubit IBM Heron `r2` chip with heavy-hex topology can accommodate two parallel chains with at most 26 qubits each. Longer chains must include a non-parallel section. For this reason, the spin orbitals of molecules with fewer than 26 MOs (52 spin orbitals) are mapped to α and β qubit registers that form two parallel chains connected by ancillas at every fourth qubit. For molecules with more than 52 spin orbitals, the two spin registers are mapped onto chains with parallel sections (longest available on the chip) and non-parallel sections. The lowest energy MOs are assigned to those parallel sections and the remaining MOs are mapped to the two non-parallel segments. Among all embeddings of these patterns into the coupling graph of the quantum chip, the one minimizing the summed two-qubit gate and readout errors of all qubits of the circuit is selected. The locality constraint of the LUCJ ansatz restricts nonzero elements of the Jastrow matrices to pairs of orbitals whose qubits are adjacent, thus conserving all $J_{p\sigma,p+1\sigma}$ same spin interaction terms and opposite-spin $J_{p\sigma,p\tau}$ terms with rungs connecting the parallel sections of the chains (every fourth orbital of these sections).

[a] Note that we do not freeze any molecular orbitals anywhere in this study.

Molecular orbital alignment

Significant QPU computational cost is associated with running different circuits for different molecular geometries at each iteration of structural relaxation or MEP calculation. Furthermore, the interdependency between the QPU and classical workloads prevents their parallel execution and thus introduces latency as jobs are queued for QPU or classical HPC execution at each iteration. It is therefore highly desirable to reuse bitstrings sampled from the circuits of a given molecular geometry for multiple iterations with slightly different molecular geometries.

Here, we label the reference molecule as A and its slightly distorted counterpart as B. The molecular orbitals defining the Hartree-Fock ground states of the two geometries $X = \{A, B\}$ in their respective atomic orbital bases are:

$$|\phi_q^{(A)}\rangle = \sum_\nu C_{\nu q}^{(A)} \, |\chi_\nu^{(A)}\rangle \,, \quad \text{and} \quad |\phi_p^{(B)}\rangle = \sum_\mu C_{\mu p}^{(B)} \, |\chi_\mu^{(B)}\rangle \tag{5}$$

And the molecular orbital bases overlap matrix between the two geometries is defined by:

$$S_{\mathrm{MO}}^{(BA)} = C^{(B)\dagger} S_{\mathrm{AO}} C^{(A)} \tag{6}$$

With atomic-bases overlap matrix elements given by:

$$S_{\mathrm{AO},\mu\nu}^{(BA)} = \langle \chi_\mu^{(B)} | \chi_\nu^{(A)} \rangle \tag{7}$$

Since the Hartree-Fock reference is invariant under unitary rotations within the occupied and virtual spaces (and, for open-shell molecules, within the singly occupied space), individual molecular orbitals are not uniquely defined and may undergo arbitrary rotations as the molecular geometry changes. Consequently, orbital identities may vary significantly and even discontinuously, despite the underlying electronic state varying smoothly. Bitstrings sampled from the circuits constructed for the reference geometry can therefore not be reused directly for its distorted counterparts.

In order to ensure that the bitstrings from the distorted geometry correspond to those sampled for the reference geometry, we rotate[32,33] the MOs of the frozen, doubly occupied, singly occupied and virtual blocks of molecule B, i.e. $C_{\mathrm{occ}}^B \to C_{\mathrm{occ}}^B U_{\mathrm{occ}}$ and $C_{\mathrm{virt}}^B \to C_{\mathrm{virt}}^B U_{\mathrm{virt}}$, where the subspace rotations U_{occ} and U_{virt} are chosen as:

$$\min_U \left(\sum_i^{N_{\mathrm{subspace}}} \left\| |\phi_i^{(A)}\rangle - |\tilde{\phi}_i^{(B)}\rangle \right\|^2 \right) \tag{8}$$

where $|\tilde{\phi}_i^{(B)}\rangle$ are the rotated MOs for each subspace. This problem is equivalent to maximizing the traces $\mathrm{Tr}(S_{\mathrm{MO}}^{(AB)} U)$ in the occupied and virtual subspaces and has the solution:

$$U = U_R U_L^T \tag{9}$$

where the matrices U_R and U_L are obtained from the singular value decompositions in each subspace:

$$S_{\mathrm{MO}}^{(AB)} = U_L \Sigma U_R^T \tag{10}$$

Nuclear gradients

Nuclear gradients are computed semi-numerically by central finite differences of the ground state energy at fixed one- and two-electron reduced density matrices (RDMs) γ and Γ, following Coe et al.[34,35]. The gradient components are given by:

$$\frac{\partial E}{\partial R_{I\alpha}} \approx \frac{1}{2h} \left[\sum_{pq} \gamma_{pq} \, \Delta h_{pq} + \frac{1}{2} \sum_{pqrs} \Gamma_{pqrs} \, \Delta(pq|rs) + \Delta E_{\mathrm{nuc}} \right] \tag{11}$$

Here the $R_{I\alpha}$ are the x, y, z coordinates of nucleus I. Hartree-Fock is solved at both displaced geometries of the finite differences evaluations, and the resulting MOs are aligned to the reference orbitals as described above. The one- and two-electron integrals are transformed to the aligned MO bases, and the gradient component is evaluated with the RDMs of the current state held fixed.

VGSQD algorithm overview

With all key components of the VGSQD algorithm introduced, we describe the full algorithm below. It can be applied to any problem where SQD is used to determine the ground state of closely related molecular geometries, such as geometry optimization, nudged elastic band (NEB) calculations and molecular dynamics (MD). A schematic of the algorithm is shown in Figure 1. The VGSQD algorithm is defined by:

(i) A Hartree-Fock calculation defines the MO basis of the reference molecule A.

(ii) A set of bitstrings $\tilde{\chi}$ is sampled from a LUCJ circuit representing the reference molecule. The ground state of the reference molecule is determined with the configuration recovery and subspace diagonalization procedure of SQD and the determinants $\{|x_i\rangle\}$ defining the corresponding subspace $\mathcal{S}$ are stored. VGSQD terminates if the optimization/NEB/MD has converged.

(iii) The optimization/NEB/MD algorithm updates the nuclear coordinates, which define the new molecule B. A Hartree-Fock calculation defines the MO basis of molecule B.

(iv) The maximally aligned rotated MO basis $\tilde{B}$ is determined and $S_{\mathrm{MO}}^{(\tilde{B}A)}$ is compared to the identity. If any component $\delta_{\mathrm{align}} = \max\left(|S_{\mathrm{MO}}^{(\tilde{B}A)} - I|_{pq}\right)$ exceeds a threshold $\epsilon_{\mathrm{align}}$ (typically 0.03), the electronic structure has changed too much for the stored samples to remain representative. $\tilde{B}$ becomes the new reference and return to step (ii). Otherwise go to (v).

(v) Compute the displacement between the two molecules $\Delta\mathbf{R} = \mathbf{R}_B - \mathbf{R}_A$. If no component of $|\Delta\mathbf{R}|$ exceeds a threshold ϵ_{pos} (typically 0.02 Å), go to step (vi). Otherwise, the ground state of $\tilde{B}$ is determined with configuration-recovery and subspace diagonalization using the reference bitstrings $\tilde{\chi}$. This step generates a new subspace $\mathcal{S}$ but still requires no quantum circuit execution. VGSQD terminates if the optimization/NEB/MD has converged; otherwise go to step (iii).

(vi) The rotated Hamiltonian is projected in $\mathcal{S}$ and diagonalized. VGSQD terminates if the optimization/NEB/MD has converged; otherwise go to step (iii).

The agreement of the molecular orbital bases between the reference and distorted molecules allows bitstrings reuse and is a useful criterion to screen out several electronic transitions. Nevertheless, it can miss electronic transitions of the many-body ground state. For this reason, resampling on the QPU (step (ii)) is also performed when $\delta_{\mathrm{CI}} = 1 - \left|\mathbf{c}^{(\mathbf{A})\dagger}\mathbf{c}^{(\tilde{\mathbf{B}})}\right|^2 > \epsilon_{\mathrm{CI}}$, with $\mathbf{c}^{(\mathbf{A})}$ and $\mathbf{c}^{(\tilde{\mathbf{B}})}$ the ground states' CI coefficients of the two molecules. This equals the infidelity between the reference and distorted molecules' ground states when the two MO bases are identical. We use $\epsilon_{\mathrm{CI}} = 0.01$.

For molecular geometry optimization, we use a trust-region version of the BFGS algorithm[36,37]. Convergence is achieved when the magnitude of all components of the forces is below 0.1 mHa/Bohr and the per-iteration energy reduction is below 1 µHa. For CI-NEB, a convergence threshold of 1 mHa/Bohr was used.

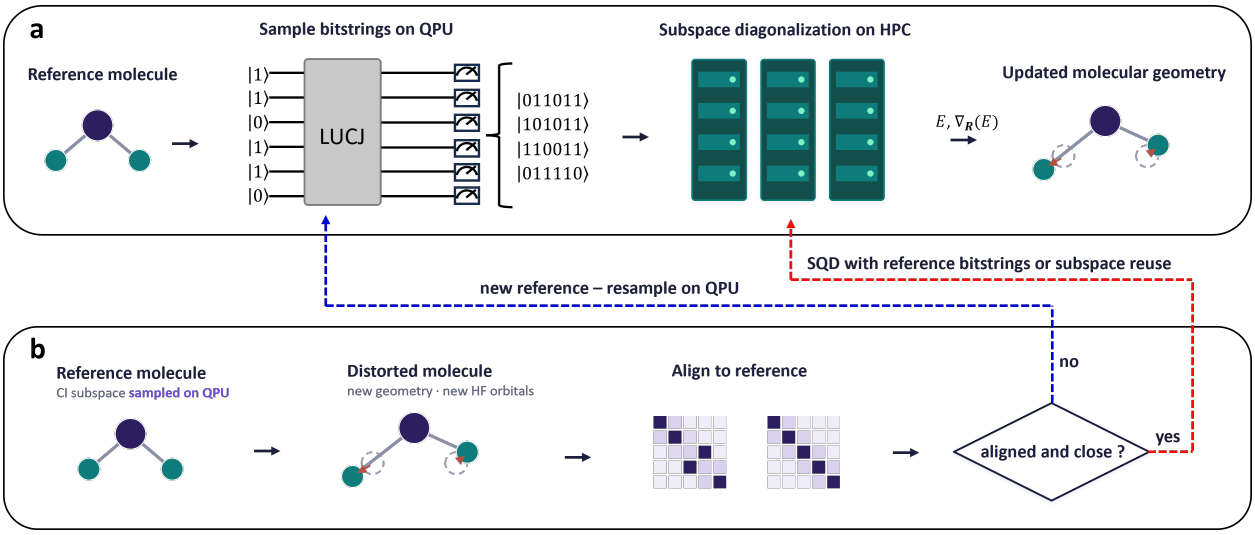

Figure 1 Schematic of the VGSQD algorithm. (a) VGSQD workflow: LUCJ circuit sampling on the QPU for the reference molecule, subspace diagonalization on HPC and geometry update. (b) Alignment of the MOs of the distorted molecule to those of the reference (MO overlap matrix before and after alignment). If the alignment and displacement criteria are satisfied, SQD is carried out with the reference bitstrings (red path); otherwise a new reference is defined and re-sampled on the QPU (blue path).

Details of the QPU execution

All our experiments were run on the `ibm-quebec` Heron `r2` device. For each LUCJ circuit, transpiled using `optimization_level=3` of the Qiskit transpiler, we carry out 256 000 shots. Given that this is a sampling-based problem, the options available for error suppression in Qiskit IBM Runtime (`v0.43.1`) are measurement twirling, Pauli twirling, and dynamical decoupling[38]. To select the best combination, we run a mirrored circuit — our circuit composed with its inverse — and measure single-Z observables on all active qubits. We test all combinations of the aforementioned error suppression strategies (including with all of them turned off), and then select the combination with mean expectation value across all observables closest to the ideal value of 1. This leads us to use only measurement twirling (enabled with the default settings in Qiskit IBM Runtime) in our experiments.

Summaries of circuit parameters and QPU performance are presented in Table 1 and Table 2. We then compute the ground state of the reference molecule using the subspace diagonalization and the self-consistent configuration recovery procedure detailed in ref. 8 and implemented using `qiskit_addon_sqd`[39] with 5 batches of up to 9000 samples at each iteration, leading to final subspace sizes of up to 9.6E7. Classical quantum chemistry computations are done using PySCF, and the diagonalization is done using DICE[40,41] on 378 vCPUs distributed across 14 compute nodes with 230 GB of memory per node of the Harfang cluster.

Results and discussion

We first examine a simple, yet challenging use case, which is the beryllium dimer (Be_2)[42]. Its weak covalent bond is driven by a delicate balance of static and dynamic correlation, making accurate bond length and energy predictions difficult for conventional classical methods. Before carrying out molecular geometry optimization with VGSQD, we validate the SQD ground state calculation and

Table 1 Circuit parameters for selected simulations presented in this work. The Be_2 rows correspond to simulations shown in Figure 2; the H_2O rows correspond to the simulations shown in Table 3 and the H_3 row corresponds to the first optimized image of the simulation shown in Figure 4.

	Number of qubits	Circuit depth	2Q depth	2Q count
Be_2 – cc-pVDZ	62	873	198	4586
Be_2 – cc-pVTZ	124	2033	477	21370
H_2O – cc-pVDZ	53	826	194	3394
H_2O – cc-pVTZ	122	2284	561	19634
H_3 – cc-pVTZ	85	2979	637	19742

Table 2 QPU performance metrics recorded from the hardware at the time of each of the calculations carried out in this work. The Be_2 rows correspond to simulations shown in Figure 2; the H_2O rows correspond to the simulations shown in Table 3 and the H_3 row corresponds to the first optimized image of the simulation shown in Figure 4. Median values ± standard deviation are reported for all qubits of the circuits for gates, and for all qubits excluding ancillas for readout.

	1Q gate time (ns)	1Q gate error (%)	2Q gate time (ns)	2Q gate error (%)	Readout time (ns)	Readout error (%)
Be_2 – cc-pVDZ	32	0.012±0.002	68	0.166±0.081	2180	0.513±0.214
Be_2 – cc-pVTZ	32	0.017±0.004	68	0.178±0.080	2180	0.610±0.317
H_2O – cc-pVDZ	32	0.015±0.004	68	0.194±0.079	2180	0.476±0.183
H_2O – cc-pVTZ	32	0.019±0.005	68	0.160±0.059	2584	0.562±0.220
H_3 – cc-pVTZ	32	0.017±0.005	68	0.205±0.087	2180	0.562±0.244

benchmark against classical methods using two basis sets: cc-pVDZ and cc-pVTZ. The cc-pVDZ basis set leads to a 62-qubit circuit (Figure 2a), whereas 124 qubits are used for cc-pVTZ (Figure 2b).

The convergence of the SQD ground state energies during the configuration recovery procedure is reported in Figure 2c and Figure 2d. For both basis sets, convergence is achieved within three iterations, followed by minor statistical fluctuations. The converged SQD ground state energies are −29.2356 Ha and −29.2486 Ha for cc-pVDZ and cc-pVTZ respectively. SQD is on par with CCSD for the larger basis set and outperforms CCSD(T)/DMRG [b] for the smaller basis set, thus validating the accuracy of SQD for the Be_2 molecule. We note that SQD slightly underperforms in comparison with CCSD(T) and DMRG for the larger, cc-pVTZ basis set. This is likely due to the corresponding quantum circuits being deeper and due to the increased memory requirements for classical postprocessing, which limited the size of the subspace onto which the Hamiltonian was projected. Nevertheless, these results suggest that Be_2 with the cc-pVDZ basis set is a strong use case to test the VGSQD algorithm.

Next, we examine the application of the VGSQD algorithm to molecular geometry optimization for the beryllium dimer with the cc-pVDZ basis set. We start the optimization from a bond length of 2.46 Å (experimental value). The energy and gradient norm are shown in Figure 3a and Figure 3b, respectively. Both quantities decrease monotonically and the optimization terminates successfully when the energy and gradient criteria are fulfilled at iteration 5. We note that each self-consistent configuration recovery and diagonalization yield a slightly different subspace. While the ground state solution in the subspace is a good approximation of the FCI solution, it only converges to the exact solution in the FCI limit. While not observed here, it can cause the energy and gradient to increase during the optimization due to a discontinuous potential energy surface[30]. Care must thus

[b] See Appendix A for the details of the DMRG calculations.

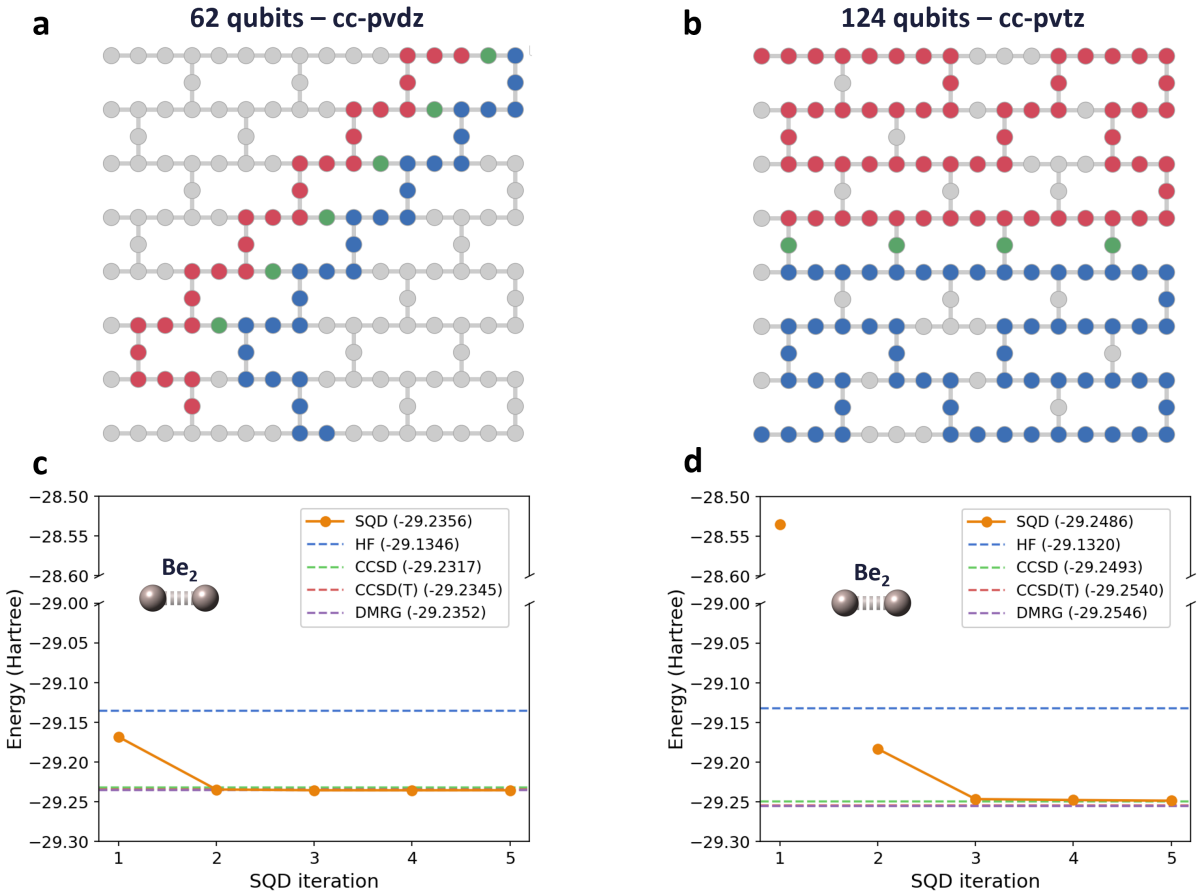

Figure 2 (a, b) Qubit layouts of LUCJ circuits of Be_2 with the cc-pVDZ (a) and cc-pVTZ (b) basis sets. Qubits used to encode the occupation numbers of α (β) spin orbitals are shown in red (blue). Ancilla qubits mediating the density–density interactions between opposite spin are shown in green. (c, d) SQD energy convergence vs. iteration of the configuration recovery procedure for Be_2 with the cc-pVDZ basis set at bond length of 2.564 Å (c) and cc-pVTZ basis set at bond length of 2.385 Å (d), with comparison to classical methods.

be taken to ensure convergence of the SQD energy *with respect to* the subspace dimension.

The MO and CI criteria during the optimization are plotted in Figure 3c. As expected, both the infidelity δ_{CI} and the MO misalignment δ_{align} increase between QPU sampling rounds, during the Be_2 molecular geometry optimization. Here, only one re-sampling on the QPU was required, as indicated by the dashed line between iteration 3 and 4 and triggered by the δ_{align} criterion. Evidently, both δ_{CI} and δ_{align} return to zero after updating the reference and resampling on the QPU, then start slowly increasing again. We note that δ_{align} increases much more rapidly than δ_{CI}, which is expected considering the translation of the nuclei. Interestingly, δ_{CI} remains very small and considerably below 10^{-3}. The agreement of the ground state CI coefficients from the two geometries confirms that the MO rotation makes the sampled bitstrings re-usable across geometries and suggests that the VGSQD algorithm converges to the ground state, even when using bitstrings sampled from another molecular geometry. Nonetheless, these criteria may not be sufficient to identify problematic electronic transitions that make the sampled bitstrings no longer re-usable in molecules with near-degenerate ground states. In those cases, the VGSQD algorithm may need to

be modified to track multiple states, including low-lying excited states, such as with the ExtSQD algorithm[17].

The results of the MO alignment procedure are shown in Figure 3(d–f). The unaligned cross-geometry MO overlap matrix $S_{\mathrm{MO}}^{(AB)}$ at iteration 4, where resampling on the QPU was triggered by the δ_{align} criterion, is shown in Figure 3d. There are large off-diagonal elements, which are mainly attributed to arbitrary rotations of the MOs within the occupied and virtual Hartree-Fock subspaces. These rotations alter the correspondence between MOs at the two geometries, making the sampled bitstrings no longer correspond to the same orbital configurations at the new geometry. The MO overlap matrix after alignment with the reference molecule's MO basis $S_{\mathrm{MO}}^{(A\tilde{B})}$ can be seen in Figure 3e. $S_{\mathrm{MO}}^{(A\tilde{B})}$ is mostly diagonal with some small off-diagonal elements (magnified by the compressed color scale range), thus indicating that correspondence between MOs at the two geometries has been restored. Here, the remaining small off-diagonal elements are expected since the MOs span slightly different subspaces because of the changes in the nuclear coordinates and resulting AO bases. As the reference molecule is updated to the new geometry and its LUCJ circuit is sampled on the QPU, $S_{\mathrm{MO}}^{(A\tilde{B})}$ returns to the identity (Figure 3f). The resulting fresh bitstrings can then be used for the subsequent geometry optimization iterations, while satisfying the δ_{align} and δ_{CI} tolerance.

The VGSQD geometry optimization results for Be_2 with the cc-pVDZ basis are displayed in Figure 3g and compared to classical methods. The geometry optimization yields unbounded monomers, rather than a weakly bonded dimer for both Hartree-Fock and CCSD. On the other hand, CCSD(T) and VGSQD recover a bound dimer as they both incorporate higher-order excitations required to describe the correlation. Interestingly, the bond length found with VGSQD (2.555 Å) is closer to the experimental value (2.46 Å) than the CCSD(T) one (2.611 Å). This improvement over CCSD(T) is consistent with the energy comparison reported in the previous section. These results support the validity of the VGSQD algorithm for molecular geometry optimization in classically challenging strongly correlated systems.

While optimizing the Be_2 bond length is a useful case study to validate the VGSQD algorithm, Be_2 only has a single degree of freedom, which makes it approachable by carrying out SQD calculations at various bond lengths to find the equilibrium interatomic distance. Nonetheless, this approach has lower accuracy and a higher quantum and classical computational cost. Furthermore, it scales exponentially with the number of degrees of freedom (DOFs). On the other hand, VGSQD can *a priori* be applied to molecules with large numbers of DOFs. Although there are no theoretical scaling laws for geometry optimization, a linear scaling of the number of iterations with the number of DOFs is generally observed[43]. Furthermore, it is reasonable to expect better scaling for VGSQD since QPU calls are needed mainly when the geometry changes significantly, which can largely be avoided by sensible initialization.

In Table 3 below, we also demonstrate the application of VGSQD to H_2O geometry optimization[c]. With the cc-pVTZ basis set, the bond length and bond angle converge to the experimental value within 0.002 Å and 0.41°, respectively. This confirms the potential of VGSQD for geometry optimization of molecules with multiple DOFs. Nonetheless, we note that CCSD(T) outperforms VGSQD on the energy prediction for both the cc-pVDZ and cc-pVTZ basis sets, as expected given that the correlation in H_2O is mainly dynamical, which is well captured by CCSD(T).

Finally, we demonstrate the application of VGSQD to chemical reactions; that is, finding their minimum energy path (MEP) and energy barrier. For this case study, we look at the $H_2+H \rightarrow H+H_2$ hydrogen exchange reaction and use the climbing image nudged elastic band method (CI-NEB)

[c]Additional convergence results are presented in Appendix B.

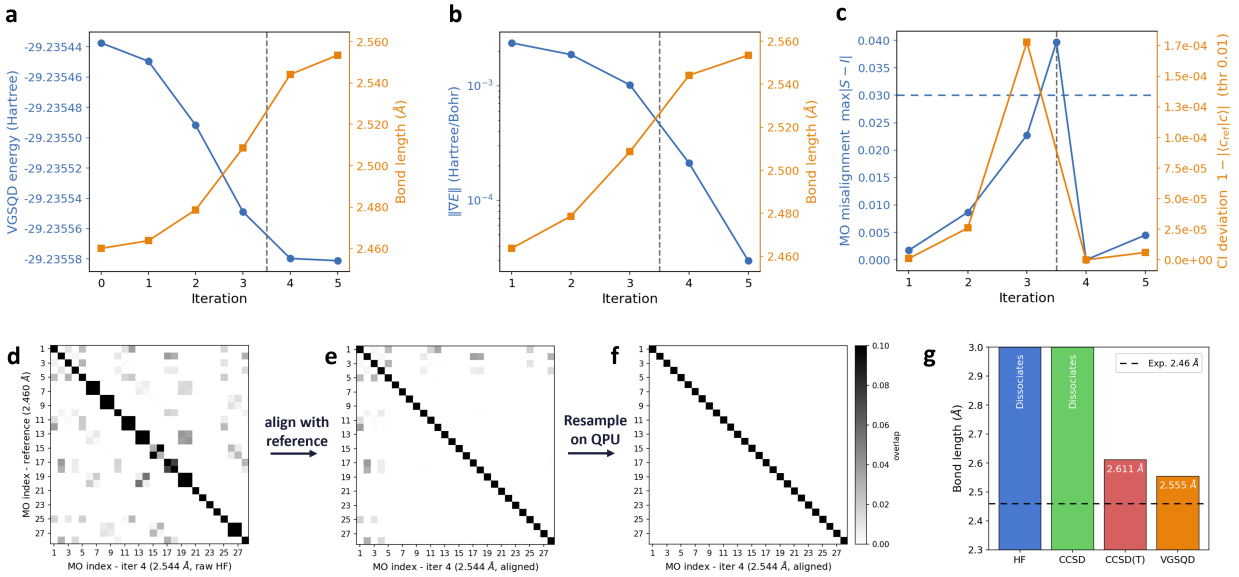

Figure 3 VGSQD geometry optimization of Be_2 with the cc-pVDZ basis set. (a, b) SQD energy (a) and gradient norm (b) vs. iteration, with the bond length shown on the right axis. (c) MO misalignment δ_{align} and CI infidelity δ_{CI} vs. iteration; the horizontal dashed line indicates ϵ_{align}. The vertical dashed lines in (a–c) mark the re-sampling on the QPU. (d–f) Cross-geometry MO overlap matrix between the reference (2.460 Å) and iteration 4 (2.544 Å) geometries before alignment (d), after alignment (e) and after re-sampling on the QPU (f). (g) Optimized bond length with comparison to classical methods and experiment.

Table 3 VGSQD energies, bond lengths and bond angles with comparison to CCSD(T) and experimental values. Energies are reported from the corresponding equilibrium geometry obtained for each method using BFGS. Experimental energies are not included since absolute electronic ground-state energies are not directly accessible experimentally. Experimental Be_2 bond angle is omitted as it is a diatomic molecule.

	Energy (Ha)	Bond length (Å)	Bond angle (°)
Be_2 experimental	—	2.460	—
Be_2 VGSQD – cc-pVDZ	−29.2356	2.555	—
Be_2 VGSQD – cc-pVTZ	−29.2485	2.383	—
Be_2 CCSD(T) – cc-pVDZ	−29.2346	2.611	—
Be_2 CCSD(T) – cc-pVTZ	−29.2541	2.340	—
H_2O experimental	—	0.958	104.48
H_2O VGSQD – cc-pVDZ	−76.2417	0.966	102.16
H_2O VGSQD – cc-pVTZ	−76.3021	0.956	104.07
H_2O CCSD(T) – cc-pVDZ	−76.2434	0.966	101.94
H_2O CCSD(T) – cc-pVTZ	−76.3458	0.958	103.68

with the cc-pVTZ basis set[d]. For each NEB image, an 85 qubit LUCJ circuit was sampled, and no resampling was triggered during the MEP optimization. While not done in this work, QPU cost could be reduced by using the same circuits for multiple images in the same, or across multiple iterations, if δ_{CI} and δ_{align} do not exceed their respective thresholds. Furthermore, the classical cost and memory scale almost perfectly linearly with the number of images, and images can be distributed across nodes with near-ideal memory distribution and speedup. Figure 4 shows the optimized MEP. The path is symmetric about the transition state, as expected from the symmetry of the reaction. The transition state converges to the collinear H_3 saddle point with an energy barrier of 9.75 kcal/mol (Figure 4a). Projecting the path onto the $r_{H_a} - r_{H_b}$ and $r_{H_b} - r_{H_c}$ coordinates shows the characteristic L-shape profile of a concerted exchange where the incoming bond contracts, while the breaking bond extends, with a saddle point H-H distance of 0.929 Å. These results are in very good agreement with FCI calculations, which yield a 9.94 kcal/mol barrier and 0.930 Å H-H distance at the saddle point with the same basis set[44].

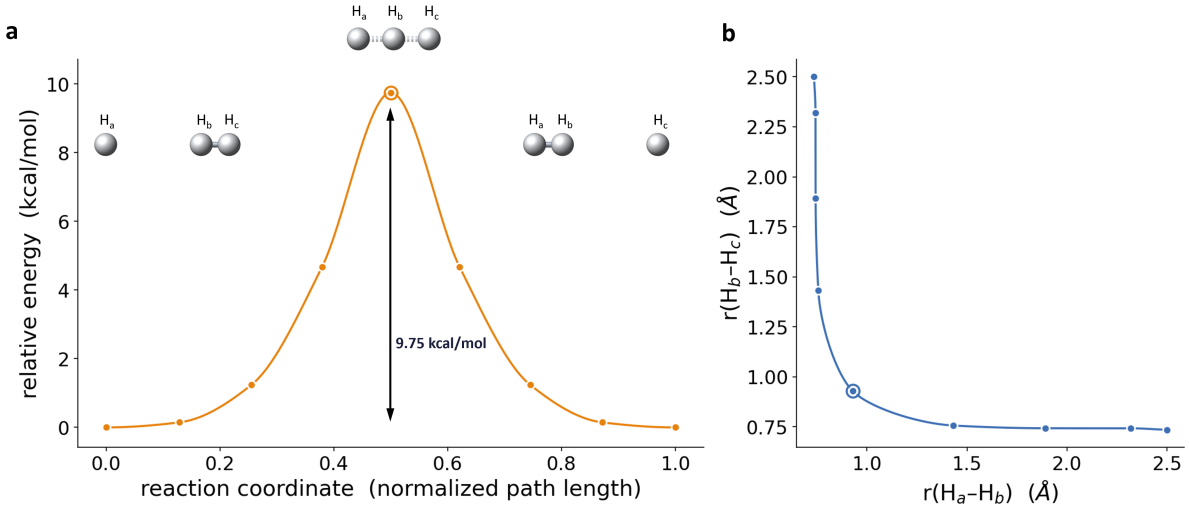

Figure 4 Minimum energy path of the $H_2 + H \rightarrow H + H_2$ reaction obtained with VGSQD and CI-NEB (cc-pVTZ). (a) Energy of the NEB images relative to the reactants vs. normalized path length, with the transition state circled. (b) Projection of the path onto the $r(H_a–H_b)$ and $r(H_b–H_c)$ coordinates.

Conclusion

In summary, we developed the variable geometry sample-based quantum diagonalization (VGSQD) algorithm, which extends SQD based algorithms and workflows to molecules with variable geometries by allowing quantum samples to be reused across multiple molecular configurations. We demonstrated the application of VGSQD to molecular geometry optimization by leveraging a quantum-centric supercomputing workflow using utility-scale quantum circuits of up to 124 qubits, run on an IBM superconducting gate-based quantum computer. The accuracy of the calculations rivals state-of-the-art classical methods such as CCSD(T) and DMRG, both for ground state energies and optimized molecular geometries. Moreover, we demonstrated that VGSQD can naturally be used to study chemical reactions and determine minimum energy paths, saddle points and energy barriers. These demonstrations broaden the scope of quantum algorithms in chemistry applications. While

[d]Additional convergence results are presented in Appendix C.

not explored in this work, VGSQD can be implemented with other ansätze than LUCJ and can be adapted to integrate with multiple other algorithms such as sample-based Krylov quantum diagonalization, TrimSQD[14], and embedding methods and thus can play a key role in current and early fault tolerant quantum-centric workflows.

Acknowledgements

The authors thank Kevin Sung, Mario Motta, and Sean Wagner for fruitful discussions and comments on the draft. The authors acknowledge access to the `ibm_quebec` system for quantum experiments and the *Harfang* cluster for classical postprocessing, through PINQ^2. The authors used generative AI tools (Claude and GPT) to assist with writing the code used in this manuscript, to generate drafts of figures and plots, to scaffold the methods section, to brainstorm about experiments and parts of the algorithm, to help with literature review, and to help with clarity, syntax, and grammar. The authors designed and carried out the core of the experiments and algorithms and maintain full responsibility for the algorithm design, its execution and all the reported results, and conclusions.

References

[1] A. Y. Kitaev. Quantum measurements and the Abelian stabilizer problem. *arXiv preprint quant-ph/9511026*, 1995.

[2] A. Aspuru-Guzik, A. D. Dutoi, P. J. Love, and M. Head-Gordon. Simulated quantum computation of molecular energies. *Science*, 309(5741):1704–1707, 2005.

[3] A. Peruzzo, J. McClean, P. Shadbolt, M.-H. Yung, X.-Q. Zhou, P. J. Love, A. Aspuru-Guzik, and J. L. O'Brien. A variational eigenvalue solver on a photonic quantum processor. *Nature Communications*, 5(1):4213, 2014. doi: 10.1038/ncomms5213.

[4] J. R. McClean, J. Romero, R. Babbush, and A. Aspuru-Guzik. The theory of variational hybrid quantum-classical algorithms. *New Journal of Physics*, 18(2):023023, 2016.

[5] A. Kandala, A. Mezzacapo, K. Temme, M. Takita, M. Brink, J. M. Chow, and J. M. Gambetta. Hardware-efficient variational quantum eigensolver for small molecules and quantum magnets. *Nature*, 549(7671):242–246, 2017.

[6] Y. O. Nakagawa, M. Kamoshita, W. Mizukami, S. Sudo, and Y.-y. Ohnishi. ADAPT-QSCI: Adaptive construction of an input state for quantum-selected configuration interaction. *Journal of Chemical Theory and Computation*, 20(24):10817–10825, 2024.

[7] M. Motta, W. Kirby, I. Liepuoniute, K. J. Sung, J. Cohn, A. Mezzacapo, K. Klymko, N. Nguyen, N. Yoshioka, and J. E. Rice. Subspace methods for electronic structure simulations on quantum computers. *Electronic Structure*, 6(1):013001, 2024. doi: 10.1088/2516-1075/ad3592.

[8] J. Robledo-Moreno, M. Motta, H. Haas, A. Javadi-Abhari, P. Jurcevic, W. Kirby, S. Martiel, K. Sharma, S. Sharma, T. Shirakawa, I. Sitdikov, R.-Y. Sun, K. J. Sung, M. Takita, M. C. Tran, S. Yunoki, and A. Mezzacapo. Chemistry beyond the scale of exact diagonalization on a quantum-centric supercomputer. *Science Advances*, 11(25):eadu9991, 2025. doi: 10.1126/sciadv.adu9991.

[9] Keita Kanno, Masaya Kohda, Ryosuke Imai, Sho Koh, Kosuke Mitarai, Wataru Mizukami, and Yuya O. Nakagawa. Quantum-selected configuration interaction: Classical diagonalization of hamiltonians in subspaces selected by quantum computers. *Phys. Rev. Res.*, 8:023268, Jun 2026. doi: 10.1103/dmn4-snfx. URL `https://link.aps.org/doi/10.1103/dmn4-snfx`.

[10] S. Piccinelli, A. Baiardi, M. Rossmannek, A. Carrera Vazquez, F. Tacchino, S. Mensa, E. Altamura, A. Alavi, M. Motta, J. Robledo-Moreno, W. Kirby, K. Sharma, A. Mezzacapo, and I. Tavernelli. Quantum chemistry with provable convergence via randomized sample-based quantum diagonalization. *arXiv preprint arXiv:2508.02578*, 2025.

[11] A. Shajan, D. Kaliakin, A. Mitra, J. Robledo Moreno, Z. Li, M. Motta, C. Johnson, A. A. Saki, S. Das, I. Sitdikov, A. Mezzacapo, and K. M. Merz, Jr. Toward quantum-centric simulations of extended molecules: Sample-based quantum diagonalization enhanced with density matrix embedding theory. *Journal of Chemical Theory and Computation*, 21(14):6801–6810, 2025. doi: 10.1021/acs.jctc.5c00114.

[12] J. Yu, J. Robledo Moreno, J. T. Iosue, L. Bertels, D. Claudino, B. Fuller, P. Groszkowski, T. S. Humble, P. Jurcevic, W. Kirby, T. A. Maier, M. Motta, B. Pokharel, A. Seif, A. Shehata, K. J. Sung, M. C. Tran, V. Tripathi, A. Mezzacapo, and K. Sharma. Quantum-centric algorithm for sample-based Krylov diagonalization. *arXiv preprint arXiv:2501.09702*, 2025.

[13] S. Piccinelli, S. Barison, A. Baiardi, F. Tacchino, J. Repp, I. Rončević, F. Albrecht, H. L. Anderson, L. Gross, A. Curioni, and I. Tavernelli. Exploring pathways towards quantum advantage in quantum chemistry: The case of a molecule with half-Möbius topology. *arXiv preprint arXiv:2603.08696*, 2026.

[14] K. M. Merz, Jr., A. Shajan, D. Kaliakin, F. Liang, Y. Otsuka, T. Shirakawa, L. Broers, H. Xu, M. Tsuji, M. Sato, S. Yunoki, R. Wakizaka, Y. Kawashima, J. Doi, H. Takahashi, T. Itoko, H. Horii, T. Pellegrini, J. Robledo Moreno, K. J. Sung, E. Fejer, R. Walkup, S. Seelam, and M. Motta. Crossing the 12,000-atom barrier with heterogeneous quantum-classical supercomputing: Quantum chemistry of protein-ligand complexes. *arXiv preprint arXiv:2605.01138*, 2026.

[15] D. Kaliakin, A. Shajan, F. Liang, J. Robledo Moreno, Z. Li, A. Mitra, M. Motta, C. Johnson, A. A. Saki, S. Das, I. Sitdikov, A. Mezzacapo, and K. M. Merz, Jr. Accurate quantum-centric simulations of intermolecular interactions. *Communications Physics*, 8(1):396, 2025.

[16] D. Kaliakin, A. Shajan, F. Liang, and K. M. Merz, Jr. Implicit solvent sample-based quantum diagonalization. *The Journal of Physical Chemistry B*, 129(23):5788–5796, 2025.

[17] S. Barison, J. Robledo Moreno, and M. Motta. Quantum-centric computation of molecular excited states with extended sample-based quantum diagonalization. *Quantum Science and Technology*, 10(2):025034, 2025. doi: 10.1088/2058-9565/adb781.

[18] I. Liepuoniute, K. D. Doney, J. Robledo Moreno, J. A. Job, W. S. Friend, and G. O. Jones. Quantum-centric computational study of methylene singlet and triplet states. *Journal of Chemical Theory and Computation*, 21(10):5062–5070, 2025. doi: 10.1021/acs.jctc.5c00075.

[19] T. Smith, T. P. Gujarati, M. Motta, B. Link, I. Liepuoniute, T. Friedhoff, H. Nishimura, N. Nguyen, K. S. Williams, J. Robledo Moreno, C. Johnson, K. J. Sung, A. A. Saki, and M. Kagele. Quantum-centric simulation of hydrogen abstraction by sample-based quantum diagonalization and entanglement forging. *arXiv preprint arXiv:2508.08229*, 2025.

[20] S. Shivpuje, T. P. Gujarati, R. Van, F. C. Pickard, IV, T. Friedhoff, I. Liepuoniute, W. Davis, G. O. Jones, and A. Galda. Sample-based quantum diagonalization methods for modeling the photochemistry of diazirine and diazo compounds. *arXiv preprint arXiv:2510.00484*, 2025.

[21] K. Yamamoto, R. Masui, T. Nakajima, M. Tsuji, M. Sato, P. Schow, L. Heidemann, M. Burke, P. Seitz, O. J. Backhouse, J. W. Pedersen, J. Children, C. Holliman, N. Lysne, D. Okuno, S. Sivarajah, D. Muñoz Ramo, A. Chernoguzov, and R. Duncan. Quantum-HPC hybrid computation of biomolecular excited-state energies. *arXiv preprint arXiv:2601.15677*, 2026.

[22] Claudia Filippi and CJ Umrigar. Correlated sampling in quantum monte carlo: A route to forces. *Physical Review B*, 61(24):R16291, 2000.

[23] H. Jónsson, G. Mills, and K. W. Jacobsen. Nudged elastic band method for finding minimum energy paths of transitions. In *Classical and Quantum Dynamics in Condensed Phase Simulations*, pages 385–404. World Scientific, 1998.

[24] G. Henkelman, B. P. Uberuaga, and H. Jónsson. A climbing image nudged elastic band method for finding saddle points and minimum energy paths. *The Journal of Chemical Physics*, 113 (22):9901–9904, 2000.

[25] G. Henkelman and H. Jónsson. Improved tangent estimate in the nudged elastic band method for finding minimum energy paths and saddle points. *The Journal of Chemical Physics*, 113 (22):9978–9985, 2000.

[26] Q. Sun, T. C. Berkelbach, N. S. Blunt, G. H. Booth, S. Guo, Z. Li, J. Liu, J. D. McClain, E. R. Sayfutyarova, S. Sharma, S. Wouters, and G. K.-L. Chan. PySCF: The Python-based simulations of chemistry framework. *Wiley Interdisciplinary Reviews: Computational Molecular Science*, 8(1):e1340, 2018.

[27] P. Jordan and E. Wigner. Über das Paulische äquivalenzverbot. *Zeitschrift für Physik*, 47(9): 631–651, 1928.

[28] E. Neuscamman. Communication: A Jastrow factor coupled cluster theory for weak and strong electron correlation. *The Journal of Chemical Physics*, 139(18):181101, 2013.

[29] Y. Matsuzawa and Y. Kurashige. Jastrow-type decomposition in quantum chemistry for low-depth quantum circuits. *Journal of Chemical Theory and Computation*, 16(2):944–952, 2020.

[30] M. Motta, K. J. Sung, K. B. Whaley, M. Head-Gordon, and J. Shee. Bridging physical intuition and hardware efficiency for correlated electronic states: The local unitary cluster Jastrow ansatz for electronic structure. *Chemical Science*, 14(40):11213–11227, 2023.

[31] Kevin J. Sung, Inho Choi, Mirko Amico, Bartholomew Andrews, Esra Ayantuna, Yukio Kawashima, Wan-Hsuan Lin, David Omanovic, Samuele Piccinelli, Javier Robledo Moreno, Abdullah Ash Saki, James Shee, Soyoung Shin, Minh C. Tran, Kento Ueda, Haimeng Zhang, and Mario Motta. ffsim: Faster simulation of fermionic quantum circuits. *arXiv preprint arXiv:2605.03123*, 2026.

[32] H. F. King, R. E. Stanton, H. Kim, R. E. Wyatt, and R. G. Parr. Corresponding orbitals and the nonorthogonality problem in molecular quantum mechanics. *The Journal of Chemical Physics*, 47(6):1936–1941, 1967.

[33] J. Olsen, K. L. Bak, K. Ruud, T. Helgaker, and P. Jørgensen. Orbital connections for perturbation-dependent basis sets. *Theoretica Chimica Acta*, 90(5):421–439, 1995.

[34] J. P. Coe, A. Moreno Carrascosa, M. Simmermacher, A. Kirrander, and M. J. Paterson. Efficient computation of two-electron reduced density matrices via selected configuration interaction. *Journal of Chemical Theory and Computation*, 18(11):6690–6699, 2022.

[35] J. P. Coe. Analytic gradients for selected configuration interaction. *Journal of Chemical Theory and Computation*, 19(3):874–886, 2023.

[36] J. D. Head and M. C. Zerner. A Broyden–Fletcher–Goldfarb–Shanno optimization procedure for molecular geometries. *Chemical Physics Letters*, 122(3):264–270, 1985.

[37] J. Nocedal and S. Wright. *Numerical Optimization*. Springer, 2006.

[38] IBM Quantum. Ibm quantum compute (formerly qiskit runtime) documentation. `https://quantum.cloud.ibm.com/docs/en/api/qiskit-ibm-runtime`, 2026. Accessed: 2026-10-02.

[39] Abdullah Ash Saki, Stefano Barison, Bryce Fuller, James R. Garrison, Jennifer R. Glick, Caleb Johnson, Antonio Mezzacapo, Javier Robledo-Moreno, Max Rossmannek, Paul Schweigert, Iskandar Sitdikov, and Kevin J. Sung. Qiskit addon: sample-based quantum diagonalization. `https://github.com/Qiskit/qiskit-addon-sqd`, 2024.

[40] A. A. Holmes, N. M. Tubman, and C. J. Umrigar. Heat-bath configuration interaction: An efficient selected configuration interaction algorithm inspired by heat-bath sampling. *Journal of Chemical Theory and Computation*, 12(8):3674–3680, 2016.

[41] S. Sharma, A. A. Holmes, G. Jeanmairet, A. Alavi, and C. J. Umrigar. Semistochastic heat-bath configuration interaction method: Selected configuration interaction with semistochastic perturbation theory. *Journal of Chemical Theory and Computation*, 13(4):1595–1604, 2017.

[42] J. M. Merritt, V. E. Bondybey, and M. C. Heaven. Beryllium dimer—caught in the act of bonding. *Science*, 324(5934):1548–1551, 2009.

[43] L.-P. Wang and C. Song. Geometry optimization made simple with translation and rotation coordinates. *The Journal of Chemical Physics*, 144(21):214108, 2016.

[44] K. A. Peterson, D. E. Woon, and T. H. Dunning, Jr. Benchmark calculations with correlated molecular wave functions. IV. the classical barrier height of the $H + H_2 \rightarrow H_2 + H$ reaction. *The Journal of Chemical Physics*, 100(10):7410–7415, 1994.

[45] H. Zhai, H. R. Larsson, S. Lee, Z. Cui, T. Zhu, C. Sun, L. Peng, R. Peng, K. Liao, J. Tölle, J. Yang, S. Li, and G. K.-L. Chan. Block2: a comprehensive open source framework to develop and apply state-of-the-art dmrg algorithms in electronic structure and beyond. *The Journal of Chemical Physics*, 159:234801, 2023. doi: 10.1063/5.0180424.

Appendix A: Details of DMRG calculations

For comparison, we include the ground-state energies of the beryllium dimer (Be_2) and water (H_2O), computed with the density-matrix renormalization group (DMRG), as implemented using the `block2` package (accessed through its `pyblock2` Python interface[45]). One- and two-electron integrals were taken from a PySCF restricted Hartree–Fock (RHF) calculation, and all calculations were all-electron (no frozen core) and spin-adapted using SU(2) symmetry. CCSD(T) energies from PySCF were computed alongside as cross-checks. Each molecule was treated in both the cc-pVDZ and cc-pVTZ bases. The resulting active spaces were: Be_2 — 28 orbitals (cc-pVDZ) and 60 orbitals (cc-pVTZ); H_2O — 24 orbitals (cc-pVDZ) and 58 orbitals (cc-pVTZ); with the two molecules having 8 (Be_2) and 10 (H_2O) electrons.

An identical 16-sweep schedule was used in all calculations, ramping the bond dimension from 250 to 1000 (the maximum bond dimension for every run) while decreasing the perturbative noise. The details are as follows:

```
bond_dims = [250]*4 + [500]*4 + [1000]*8  # 16 sweeps, ramping M
noises    = [1e-4]*4 + [1e-5]*4 + [1e-6]*4 + [0.0]*4
thrds     = [1e-10]*16  # Davidson threshold
tol       = 1e-8        # sweep energy convergence
```

The DMRG ground-state energies are reported in Table 4.

Table 4 Reference DMRG ground-state energies ($M = 1000$, SU(2) spin-adapted), with RHF and CCSD(T) references. All energies are in hartree, reported to 4 decimal places. All distances and coordinate values are reported to 3 decimal places.

Molecule	Basis	R (Å)	RHF	CCSD(T)	DMRG (M=1000)
Be_2	cc-pVDZ	2.564	−29.1346	−29.2345	−29.2352
Be_2	cc-pVTZ	2.385	−29.1320	−29.2540	−29.2546
Molecule	Basis	Coordinates (Å)	RHF	CCSD(T)	DMRG (M=1000)
H_2O	cc-pVDZ	O: (0, 0, 0); H: (±0.750, 0.608, 0)	−76.0262	−76.2434	−76.2440
H_2O	cc-pVTZ	O:(0, 0, 0); H: (±0.754, 0.588, 0)	−76.0572	−76.3458	−76.3458

Convergence note. All DMRG calculations were run on an Apple M4 pro, multi-threaded across 8 threads. At the reported precision of four decimal places, all DMRG energies are fully converged with respect to bond dimension: the truncation errors lie three or more orders of magnitude below the last reported digit (the discarded weights $\lesssim 10^{-7}$, which correspond to errors of at most tens of μHa). For the specific case of Be_2 in the cc-pVDZ basis set, we empirically verified this as well, by repeating the calculation at $M = 2000$ and $M = 3000$. Orbital reordering using the `fiedler` and `gaopt` algorithms also did not change the reported energy in this case.

Appendix B: Convergence of H2O calculations

The convergence of the gradient during the VGSQD geometry optimization of H_2O presented in Table 3 is shown in Figure 5 below.

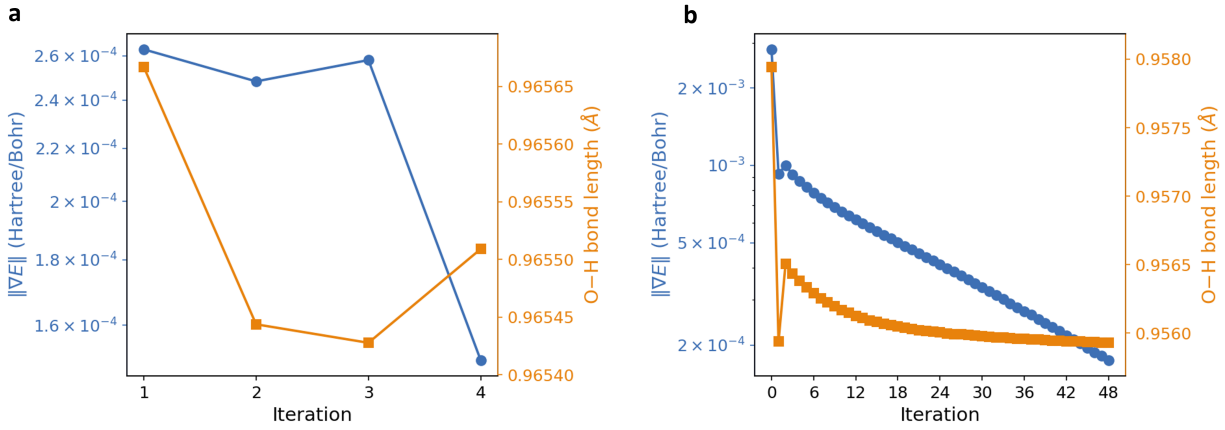

Figure 5 Gradient convergence for the VGSQD geometry optimization of H_2O with (a) the cc-pVDZ basis set and (b) cc-pVTZ basis set.

Appendix C: Convergence of CI-NEB calculations

The convergence of the gradient and barrier height during the VGSQD CI-NEB calculation of the $H_2 + H \rightarrow H + H_2$ reaction presented in Figure 4 is shown in Figure 6 below. We note that the molecular geometries of the initial path at which the VGSQD CI-NEB calculation is started were determined using a Hartree-Fock CI-NEB calculation.

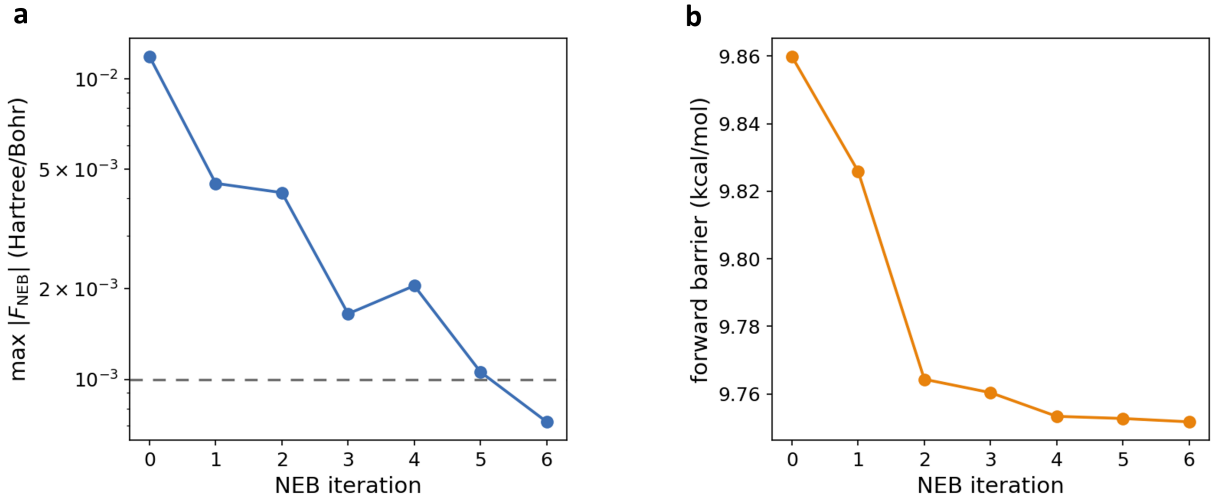

Figure 6 Convergence of the CI-NEB calculation for $H_2 + H \rightarrow H + H_2$ showing the convergence of the forces in (a) and of the barrier height in (b).